RESEARCH PAPER

CrossMark

Arrays of high aspect ratio magnetic microstructures for large trapping throughput in lab-on-chip systems

Samir Mekkaoui[1] · Damien Le Roy[2] · Marie-Charlotte Audry[1] · Joël Lachambre[3] · Véronique Dupuis[2] · Jérôme Desgouttes[1] · Anne-Laure Deman[1]

Abstract

Here we report a novel technology to obtain arrays of highly efficient magnetic micro-traps that relies on simple fabrication process. Developed micro-traps consist in chains of iron particles diluted in polydimethylsiloxane (PDMS). We analyzed the microstructure of the composite membrane by X-ray tomography. It revealed the predominance of aligned chain-like agglomerates. Largest traps, with diameter ranging from 4 to 11 μm, are found to be the most efficient. The trap arrays were characterized by a density of 1300 magnetic micro-traps/mm², an average nearest neighbor distance of 21 μm. Implemented in a microfluidic channel operating at a relatively high flow rate of 0.97 μL/s—a flow velocity of 8.3 mm/s—we measured a trapping efficiency of more than 99.7%, with a throughput of up to 7100 trapped beads/min. These performances are competitive with other approaches like hydrodynamic trapping. The strengths of this technology are its simple fabrication and easy handling.

Keywords Lab-on-Chip · Magnetophoresis · Self-organization · Single cell analysis

1 Introduction

Lab-on-chip (LOC) technology brings numerous benefits for biomedical and environmental applications. LOC significantly reduces the amount of biological sample and reagent, the cost and the time of analysis, and it enables individual cell investigations. One of the most appealing potential of LOC is certainly the development of delocalized analysis solutions, performed in laboratories. For biomedical purpose, LOC working principle involves the manipulation of cells or functionalized beads, generally seeking either high throughputs or precise positioning and manipulation of single objects. In this scope, various solutions, including hydrodynamic, optical, dielectrophoretic, magnetic or

acoustic actuations were developed. B. Cetin et al. (Cetin et al. 2014) made an extensive comparison of these techniques based on their implementation, microfabrication and materials and their performances, in particular throughput, considering clinical and diagnostic applications. All techniques present advantages or drawbacks that are weighted differently according to the use. When seeking for high-sorting throughputs, hydrodynamic, acoustic and magnetic approaches are the most competitive. Single cell analysis also represents a strong challenge and aroused great interest in the LOC community during the past 10 years (Hosic et al. 2015; Narayanamurthy et al. 2017). Indeed, as opposed to global studies of large population, single cell analysis can reveal the dispersion of individual cell characteristics, cell cycle stages, or rare cell event (Hosic et al. 2015; Yesilkoy et al. 2016; Narayanamurthy et al. 2017). Similarly, manipulation of single microbeads has attracted a lot of interest recently (Kim et al. 2012; Tekin and Gijs 2013; Xu et al. 2013). Functionalized microbead arrays are indeed powerful tools to detect and quantify biological target (proteins, RNA, DNA, etc.) or to trap labeled cells. The hydrodynamic contact-based approach has been widely developed to trap single microbeads or cells (Chen et al. 2015; Yesilkoy et al. 2016; Delapierre et al. 2017). In these works, precisely designed

✉ Samir Mekkaoui
samir.mekkaoui@univ-lyon1.fr

1 Institut des Nanotechnologies de Lyon INL-UMR5270, CNRS, Université Lyon 1, 69622 Villeurbanne, France

2 Institut Lumière Matière ILM-UMR 5306, CNRS, Université Lyon 1, 69622 Villeurbanne, France

3 Laboratoire Matériaux, Ingénierie et Sciences (MATEIS), INSA-Lyon, CNRS, UMR 5510, 20 Av. Albert Einstein, 69621 Villeurbanne, France

vertical traps (microwells) or lateral traps (U-shaped microstructures, pockets) were used. V. Narayanamurthy et al. (Narayanamurthy et al. 2017) have recently reviewed current achievements in microfluidics hydrodynamic trapping for single cell analysis. Even though this approach presents advantages, some limitations exist. Hydrodynamic methods can require sophisticated fabrication processes owing to trap dimensions and target specific geometries. Fluidic flow disturbances inherent to trap footprints must be considered when designing trapping functions. Dedicated pumping systems and fluidic controls are often needed and add complexity in the device handling.

Magnetic forces can be promising for single objects trapping. This approach is based on *magnetophoresis* which refers to the motion of an object in a non-uniform magnetic field. Magnetophoresis was implemented in LOC systems (Dempsey et al. 2007; Li et al. 2011; Rasponi et al. 2011; Forbes and Forry 2012; Marchi et al. 2015), to concentrate, separate or trap magnetically labeled cells (Yu et al. 2011), deoxygenated red blood cells (Nam et al. 2013), or functionalized magnetic microbeads (Saliba et al. 2010). The magnetic method does not require cumbersome and specialized equipment which is of first interest for applications in biological or medical laboratory. Indeed, magnetic forces can be generated by using either a simple external (bulk) permanent magnet (Mohamadi et al. 2015) or by a micrometer-sized magnetic structure nearby or within the microfluidic channel (Esmaeilsabzali et al. 2016). The latter approach permits to obtain larger magnetic field gradients, thus larger magnetic forces (Le Roy et al. 2016a, b) and to design target-size traps. Literature can be divided into two distinct kinds of micromagnets, either made of hard magnetic materials (Dumas-Bouchiat et al. 2010; Arnold and Wang 2009), or soft magnetic materials (Dempsey et al. 2014; Deman et al. 2017; Jung et al. 2010). Hard micromagnets can be permanently magnetized and therefore work autonomously. However, they generate fixed force pattern. In addition, their fabrication is usually more complex, as their magnetic performances highly depend on the material structure and microstructure (Zanini et al. 2011). In contrast, soft micromagnets need an external magnetic field in order to create a local stray field gradient, but they offer an easy modulation of the force intensity during experiments. They also imply easier fabrication process. Usually, Ni or permalloy thin films are patterned by lithography to obtain micromagnets typically 5–100 µm in size (Chen et al. 2014; Jaiswal et al. 2017; Henighan et al. 2010). These film-based processes still require several manufacturing steps, and face challenges related to the heterogeneous integration of magnetic materials with polymers, mainly polydimethylsiloxane (PDMS), such as tedious alignment procedures (for locating the traps in the channels) and tightness issues. Micromagnet arrays were reported to serve as magnetic tweezers for precise manipulation of magnetic beads or cells (Henighan et al. 2010; Rampini et al. 2016), to trap rare cells (Chen et al. 2014) or for single cell analysis (Jaiswal et al. 2017).

Here we propose a novel technology to obtain arrays of efficient magnetic micro-traps. The traps consist in high aspect ratio agglomerates of magnetic particles diluted in a polymer matrix. The magnetization and magnetic susceptibility are the two key parameters of soft micromagnets as they determine the maximum reachable force. We have chosen iron to take benefit of its high magnetization. Through the formation of high aspect ratio agglomerates we induced an increased effective magnetic susceptibility (Khashan and Furlani 2014; Le Roy et al. 2016). This novel technology, inspired by composite-polymer approach (Faivre et al. 2014; Zhou and Wang 2016; Royet et al. 2017), is low cost and requires simple fabrication process that breaks with standard microfabrication approaches. We obtained an array of 1300 magnetic micro-traps/mm^2, 4–11 µm in diameter, spaced with an average nearest neighbor distance, center-to-center, of 21 µm. In this study, we characterized the composite structure using X-ray tomography and atomic force microscopy (AFM). We characterized the trapping performances when implemented in microfluidic channel, with model superparamagnetic beads. Our findings show high trapping efficiencies (higher than 99.7%) at flow rates of 0.83 and 0.97 µL/s, respectively, flow velocities of 8.3 and 9.7 mm/s. We measured throughputs up to 7100 trapped beads/min. Considering the achievable trap size and areal density, these materials could be used for single cell assays. The final part of this report is dedicated to this application, notably assessing the fraction of traps occupied by single objects.

2 Microfabrication technology

2.1 Device fabrication

The composite (I-PDMS) was obtained through the mixture of carbonyl iron microparticles (Fe–C dry powder, 0.5–7 µm diameter, 97% Fe basis, Sigma-Aldrich) and PDMS elastomer (10/1 ratio of monomer and curing agent, respectively, Sylgard from Samaro). They were mixed in a mortar for around 4 min until obtaining a visually homogeneous material. Figure 1 shows the fabrication steps. Composite membranes were patterned using 100-µm-thick molds made of adhesive Kapton film (Adicaz, France), cut by xurography technique (Renaud et al. 2015) and bonded on silanized glass slice. Here, the dimensions of the molds were 10 mm × 10 mm in order to implement a trapping area large enough to capture thousands of beads, but not too long for the convenient of data analysis. Depending of the application, larger or smaller trapping area could be designed.
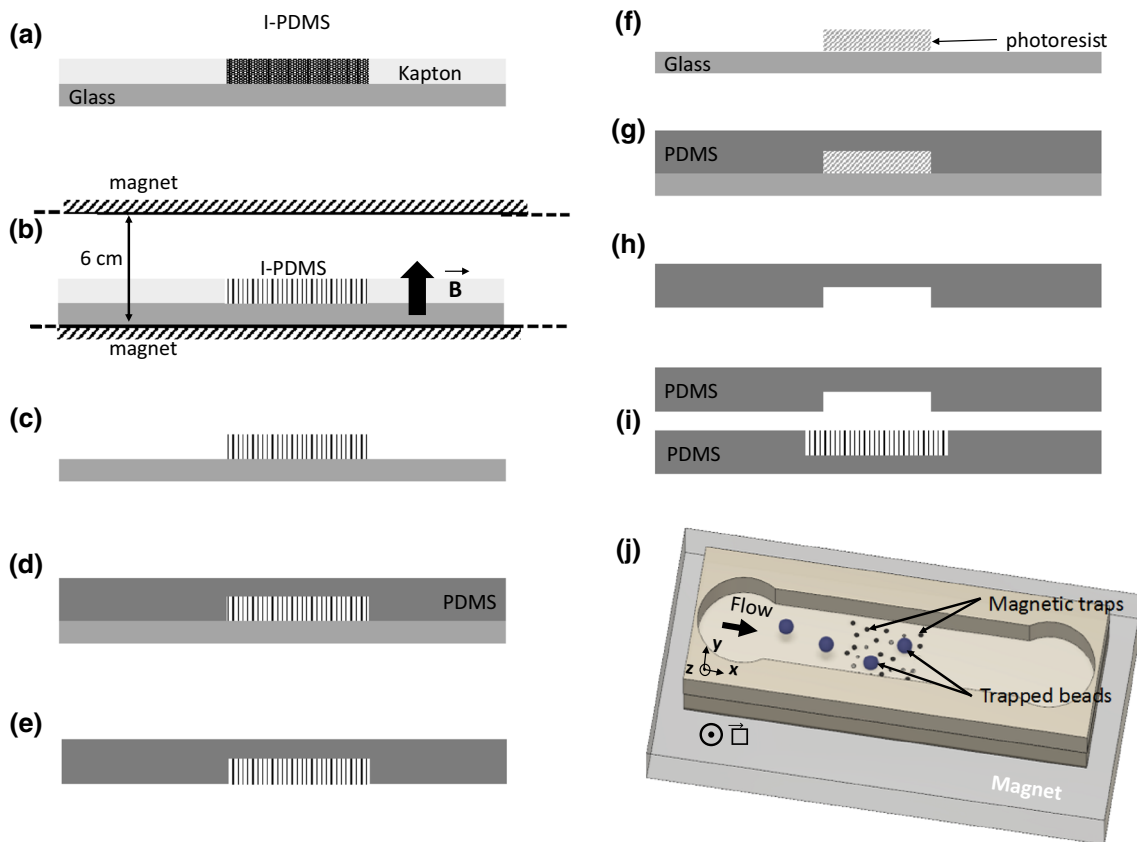
Fig. 1 Fabrication process: **a–i** are cross-sectional view, **j** 3D view of the device. **a** A Kapton film is patterned on a glass slide and I-PDMS (1 wt% or 5 wt%) is poured in the pattern. A blade is used to remove the excess of composite. **b** The I-PDMS is cured for 3 h at 70 °C between two magnets facing each other in an attractive setting to form an homogeneous vertical magnetic field of $B = 130$ mT, in order to self-organize Fe–C particles in the PDMS matrix. **c** The Kapton film is removed leaving only the self-organized composite membrane. **d** PDMS is poured on the membrane, then cured for 3 h at 70 °C. **e** The PDMS/I-PDMS membrane is unmolded. **f** The microfluidic channel mold is obtained through photolithography. **g** PDMS is poured on the mold to replicate the mold and **h** unmolded. **i** O_2 plasma bonding is performed to seal the device comprising the microfluidic channel and the composite membrane. **j** 3D representation of bead trapping in the microfluidic channel. High aspect ratio agglomerates are oriented along z axis. The magnet ($6 \times 3 \times 1.5$ cm^3) is polarized along z axis

In our previous work, we reported on the formation of high aspect ratio agglomerates of Fe–C particles within the PDMS matrix when applying a homogeneous magnetic field during curing (Le Roy et al. 2016). Both the size of the agglomerates and their distribution change with Fe–C concentration.

In the present study, we seek for the formation of dense arrays of magnetic structures characterized by a size and a pitch comparable with typical cell size (10–30 μm). Therefore, we selected concentrations of 1 and 5 wt% that lead to arrays of well-defined and isolated Fe–C agglomerates. The microstructure of these composites is further described in the "Results and discussion" section.

A magnetic field was applied during the composite reticulation for 3 h at 70 °C (Fig. 1a, b). Homogeneous magnetic field was supplied by a pair of NdFeB permanent magnet of $10 \times 11 \times 2.5$ cm^3, facing each other in an attractive configuration. They are separated by a gap of

6 cm. The mold containing the composite was positioned onto one magnet, where a magnetic field of 150 mT was measured using a Keithley Teslameter. At the position of the composite (1 mm from the magnet surface), the magnetic field gradient is 0.25 T/m, as calculated using Comsol® simulation tools. One can notice that a curing temperature of 70 °C, which is the usual curing temperature for PDMS, was chosen. Lower temperature has not shown changes in the composite microstructure, but increased the curing time. Higher curing temperature, considering temperatures compatible with PDMS, would permit to accelerate the curing process but we limited the treatment temperature to 70 °C to remain well below the Curie temperature of the $Nd_2Fe_{14}B$ phase ($T_C = 315$ °C) (Coey 2011) and thus benefit from the large stray field of the permanent magnet set-up. After reticulation, the Kapton mold was then peeled off with a tweezer, leaving a 100-μm-thick patterned composite membrane (Fig. 1c).

Pure PDMS (10/1 ratio of monomer and cross-linking agent) was poured on the composite, cured at 70 °C for 3 h, and peeled off from the glass slice to obtain a 2-mm-thick PDMS/composite membrane (Fig. 1d, e).

We patterned channels in pure PDMS matrix following a conventional soft-lithography process (Xia and Whitesides 1998; Mc Donald et al. 2000), using a 50-µm dry photoresist (Ethertec®) (Fig. 1f–h). Channel dimension was 100 µm thick (two layers of photoresist) and 1000 µm width. We sealed the channel with the as-prepared magnetic membranes using O_2 plasma bonding (Fig. 1i). A schematic of the microfluidic system illustrating bead trapping on the composite membrane is shown in Fig. 1j.

2.2 Material and experimental set-up

The inner structure of the composite was characterized using X-ray tomography. These experiments were conducted on I-PDMS with 1 wt% and 5 wt% Fe–C particles. We used "EasyTom Nano" µCT tomograph from "RX Solutions" company. The X-ray source is a LaB6 cathode with a diamond window to allow higher flux (20 µA) and the used focal spot is 0.25 µm width knowing that scans are done with a 0.3 µm voxel size. As Fe–C is quite absorbent, a tension of 90 kV is applied. A CCD detector with a matrix of 2000×1312 pixel was used to take projections over 1400 angular positions. After reconstruction, a volume of $1800 \times 1100 \times 240$ vx, i.e., $540 \times 330 \times 72$ µm³, is obtained. Post-treatment is done using ImageJ software to characterize spatial organization of the particles and to get a 3D picture of the sample. Composite topographies were recorded with AFM (Asylum Research MFP-3D) in the tapping mode with silicon probes of nominal radius of curvature 10 nm and nominal spring constant 42 N/m.

Concerning trapping function evaluation in microchannel, superparamagnetic microbeads (average diameter: 12 µm, density: 1.1 g/cm³, magnetization: 0.55 kA/m, material: magnetite nano-inclusions in a polystyrene matrix, Kisker®) were suspended in a filtered phosphate buffered saline (PBS) (viscosity: 1 mPa.s at 20 °C, pH: 7.4 and salinity: 300 mOsmol, Invitrogen®) with a concentration of 10^3 beads/µL. During the experiment, the microfluidic channel was positioned on an NdFeB magnet ($6 \times 3 \times 1.5$ cm³). It generated a magnetic field in the channel, i.e., at 2 mm from the magnet surface, of 300 mT (measured using a Keithley Teslameter). A 3D representation of the device is shown Fig. 1j. Characterization of bead trapping and release was realized using a microscope (Olympus BX51M) and recorded using a camera (Moticam2000, Motic). Obtained images were analyzed using ImageJ® software.

3 Results and discussion

3.1 Composite microstructuration

Under an external magnetic field, carbonyl iron particles can be seen as an ensemble of aligned magnetic dipoles. Before complete PDMS reticulation, the particles are allowed to move within the polymer, and their motion is governed by dipolar interactions and gravity. Adjacent particles are attracted along the flux lines and repelled in the orthogonal directions. These directional interactions lead to the formation of high aspect ratio agglomerates along the flux lines, homogeneously distributed within the matrix. Figure 2 displays reconstructed 3D profiles from X-ray tomography performed on a volume of $540 \times 330 \times 72$ µm³. The deduced Fe–C particles size, ranging from 0.5 to 6 µm, is in good agreement with our SEM (scanning electron microscopy) observations. For both concentrations, 1 wt% and 5 wt%, the tomography images revealed two types of organizations: expected chain-like agglomerates (CA), but also isotropic agglomerates (IA). CA only represent 42% of all agglomerates in both 1 wt% and 5 wt% composites but contain 92% and 96% of the total amount of Fe–C particles, respectively. IA sizes are found to be less than 6 µm, and mostly localized at the bottom of the membrane (Fig. 2b). Since the magnetic field gradient during cross-linking is rather small, 0.25 T/m (calculated using Comsol® simulation tools), we believe that this concentration of IA at the bottom mainly originates from the gravitational force.

When implemented into microfluidic devices, these agglomerates locally generate magnetic field gradients and then serve as magnetic traps. Figure 2c displays top views of the composite membranes, showing the traps distribution. Considering a random distribution of N dots in a square area of size L, the distribution of the nearest neighbor distance follows a Poisson distribution, of unique parameters N and L (Portemont 2006). The model of random distribution fails to describe the experimentally determined distribution of nearest neighbor distances, as shown in Fig. 5 for the 5 wt% composite. This suggests a partial ordering of the magnetic agglomerates, as expected from repelling force between adjacent objects with parallel magnetization. We used AFM to investigate the composites surfaces roughness. The 1 wt% and 5 wt% membranes exhibited an average roughness of 6 nm (50 nm peak–peak) and 13 nm (100 nm peak–peak), respectively. Although the 5 wt% composite is twice as rough as the 1 wt% composite surface, it remains relatively smooth as compared to the dimensions of the target objects (> 10 µm) (Fig. 3).

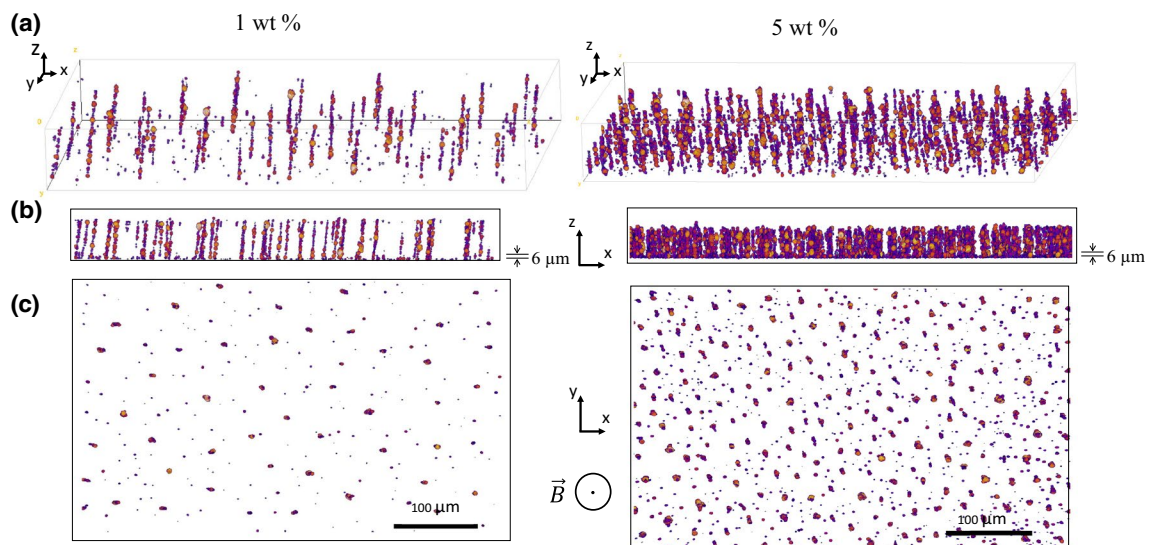We found that 1 wt% and 5 wt% composites are characterized by densities of around 1500 traps/mm² and 5000

Fig. 2 Reconstructed views from X-ray tomography performed on a volume of $540 \times 330 \times 72$ μm³ of one representative membrane for each concentration, 1 wt% and 5 wt%. **a** 3D view reconstructed with ImageJ volume viewer and projections on **b** XZ plane, the cropped 6-μm-thick superficial layer allowing to remove IA located in the bottom of the sample are indicated, and **c** XY plane showing all traps regardless of their morphology
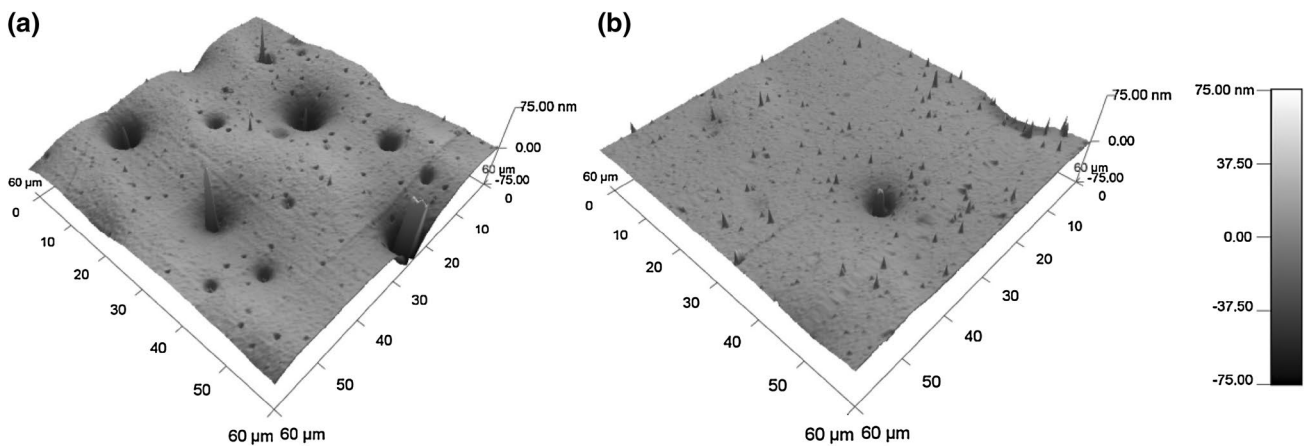

Fig. 3 Surface profile measured with AFM of **a** 5 wt% composite and **b** 1 wt% composite

traps/mm², respectively, without distinction between CA and IA. Figure 4 shows that the distribution of trap diameters exhibits two maxima, centered at 2 and 7 μm in both composite concentrations. In the following discussion, for the sake of simplicity, we will refer to two populations of traps, "small traps" and "large traps", corresponding to both peaks of the size distribution, the discriminating diameter being 4 μm. Small traps are predominant as they represent almost 81% of traps at 1 wt% composite and 74% of traps at 5 wt%. To relate the CA and IA structures to the trap size, we reconstructed a new batch of tomography images after cropping a 6-μm-thick superficial layer in the ZX plane of all images, so as to remove IA (Fig. 2b). The resulting cropped images permit to specifically characterize CA structures. Figure 4a reports the diameter distribution from IA and CA structures for 1 wt% and 5 wt% composite membranes. At 5 wt% the proportion of thicker CA structures is slightly increased, as observed by other groups (Ghosh and Puri 2013; Günther et al. 2011). Most of IA structures, 94–97% for each composite, gave rise to "small traps". Figure 4b shows the proportion of traps originating form IA and CA structures based on the discriminating diameter of 4 μm for small and large traps. 90% of large traps observed on the membrane surface originate from CA structures.

Fig. 4 **a** Distribution of trap diameters of 1 wt% membrane (top) and 5 wt% membrane (bottom), in black the IA proportion and in grey the CA proportion. **b** Pie charts showing the trap size distribution depending on their structure, in black the proportion of IA and in grey the proportion of CA. The checkerboard pattern represents all traps exhibiting a diameter $D > 4$ μm (large traps)
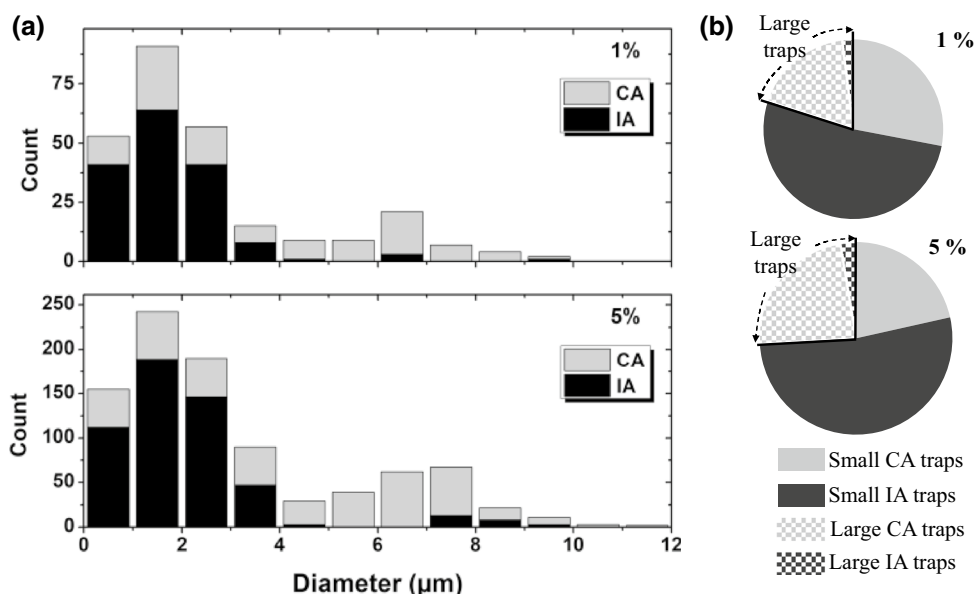
Using optical microscopy at a magnification of x100, which possesses a lower resolution compared to X-ray tomography, only larger traps are visible. Microfluidic observations realized with an optical microscope have shown that trapping only occurred on visible traps, i.e., larger traps that originate for 90% of them from CA structure. This is consistent with the fact that this structure is expected to be more efficient. Indeed, the high aspect ratio of CA structures favors the concentration of magnetic field lines (Khashan and Furlani 2014). Considering that (1) the density of traps is of first importance in the trapping capacity of the device, and (2) larger traps are the efficient ones, we focused on large traps, 4–11 μm in diameter, of the 5 wt% samples. Their density reaches 1300 traps/mm^2 with nearest neighbor distances center-to-center ranging from 17 to 27 μm as reported in Fig. 5. This trapping array specification suits not only our bead models (12 μm diameter), but also larger targets such as white blood cells (WBCs), or cancerous cells.

3.2 Trapping characterization in microfluidic channel

In our experimental set-up, the microfluidic device is positioned on an NdFeB magnet that generates a 300-mT magnetic field in the channel, i.e., at 2 mm from the magnet surface. From COMSOL® simulations, we expect a 18.2 T/m magnetic field gradient originating from the magnet underneath the device. In order to estimate the effect of the magnet alone, we first carried out a series of five experiments without magnetic composite. We observed 1–6 (an average of 3) immobilized beads in frame at 0.14 μL/s and none at 0.28 μL/s, on pure PDMS floor. This reference series of
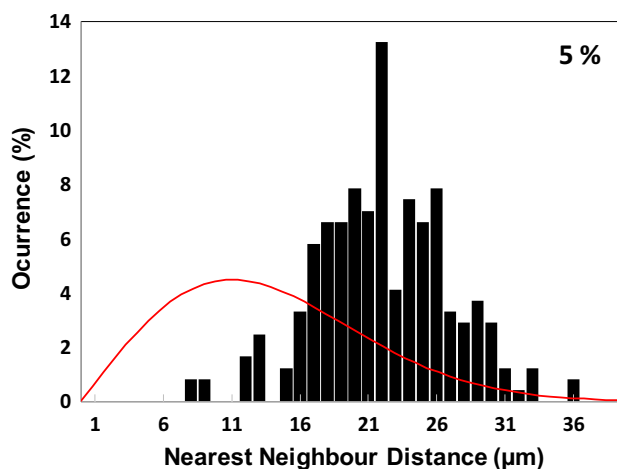
Fig. 5 Nearest neighbor distances, center-to-center, for large traps (diameter > 4 μm) of 5 wt% composite, obtained via ImageJ's NND plugin. Curve in full line represents a random distribution of $N = 242$ traps in a 0.18 mm^2 square frame

experiment ensures that in the following study, the trapping can be attributed to the composite membrane.

I-PDMS membranes containing 5 wt% Fe–C particles were then implemented into three microfluidic devices as represented in Fig. 1j. The trapping area covered the entire width of the channel (1 mm) and was extended over a length of 10 mm. The solution containing superparamagnetic beads was injected at flow rates ranging between 0.28 and 0.97 μL/s corresponding to flow velocities ranging between 2.8 and 9.7 mm/s.

A first batch of 14 experiments was carried out to study the trapping performance based on direct microscopic observation. We systematically observed two sequential regimes

of trapping. At first, injected beads are trapped, gradually filling the trapping area. The second step begins once some beads occupy the last sites of the trapping area (farthest sites from the channel entrance). Injected beads then either pass downstream the trapping region, or are captured onto unoccupied sites.

The duration of the first step inversely scales with the flow rate. At the highest considered flow rates, it remained superior to 1 min. In this initial regime, all beads were trapped for flow rates below 0.83 μL/s. In contrast, few injected beads were not trapped at 0.83 μL/s and 0.97 μL/s. We focused on these flow rates, as they constitute the best compromise between high throughput and trapping efficiency.

In a series of four additional experiments at these selected flow rates, we intended to quantify the trapping efficiency during the first step. We counted the number of beads that were not trapped, and after the flow was stopped, we took images along the trapping area to determine the number of captured beads. Figure 6a shows images of the channel before and after the experiment. The number of trapped beads was determined by post-analysis treatment using ImageJ. For sites occupied by several beads, we estimated the number of beads from the section of the beads' cluster. Table 1 shows the trapping efficiency, throughput, density of trapped beads, and ratio of traps occupied by one single bead, at 0.83 and 0.97 μL/s.

Devices demonstrated a very high trapping efficiency, superior than 99.7%, and permitted to trap up to 750 beads/mm^2. Experiments lasted about 1 min, and we obtained throughput as high as 7100 trapped beads/min. These performances are competitive with the ones recently reported for hydrodynamic approaches (Narayanamurthy et al. 2017). However, all the traps are not occupied, and beads are trapped either individually or in clusters.

We investigate the heterogeneous distribution of the trapped beads along the channel. An average of 25% of the traps are occupied by single beads or clusters of beads in the total area, but 41% at its entrance and 5% at its end. Figure 7 reports the number of trapped beads at different positions in the channel. The dimensions of each observation window are 750 μm long and 1000 μm width, which corresponds to the channel width. They are numbered form N1 to N5, as represented in Fig. 7a. For a flow velocity of 8.3 mm/s (flow rate of 0.83 μL/s), the number of trapped beads decreases from 1085 (13.6% of the total of trapped beads) in N1, to 591 (7.4%) in N3 to 150 (1.9%) in N5.

Besides trapping dynamic, theses arrays of magnetic structures could be used to immobilize single objects, notably for assays on large populations of individual cells. In this view, we focussed on the fraction of single beads occupying traps. With flow velocities of 8.3 mm/s and 9.7 mm/s, 28% and 46.7% of the traps were occupied by a single bead, the
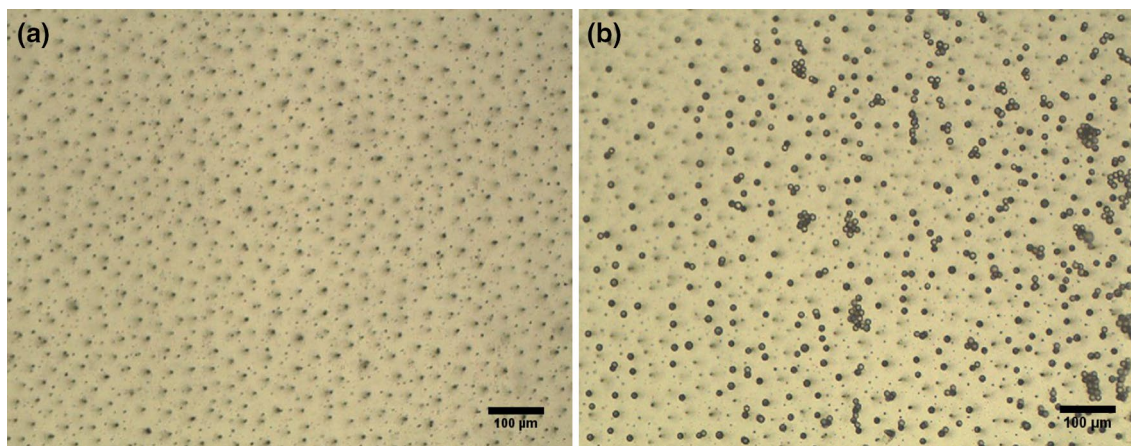

Fig. 6 Microscopic images of the trapping area **a** before and **b** after capture of the beads at a flow velocity of 9.7 mm/s (0.97 μL/s)

Table 1 Composite membrane trapping characteristics: throughput, trapping efficiency, number and density of trapped beads, ratio of traps occupied with a single bead, at flow rates of 0.83 and 0.97 μL/s, which correspond to flow velocities of 8.3 and 9.7 mm/s

Flow rate, μL/s	Velocity, mm/s	Throughput, beads/min	Trapping efficiency (%)	Number of trapped beads	Density beads/mm^2	Traps with single bead (%)
0.83	8.3	7100 +/− 500	99.94	7951 +/− 562	750 +/− 57	28
0.97	9.7	4733 +/− 338	99.77	5646 +/− 413	656 +/− 41	46.7

Measurement errors are related to the estimation of the number of captured beads in clusters

Fig. 7 **a** Schematic representation of observation windows, N1, N2, N3, N4 and N5, positioned at 0 μm, 2250 μm, 4500 μm, 6750 μm, 9250 μm from the entrance of the trapping area; **b** number of trapped beads in the channel in each observation window
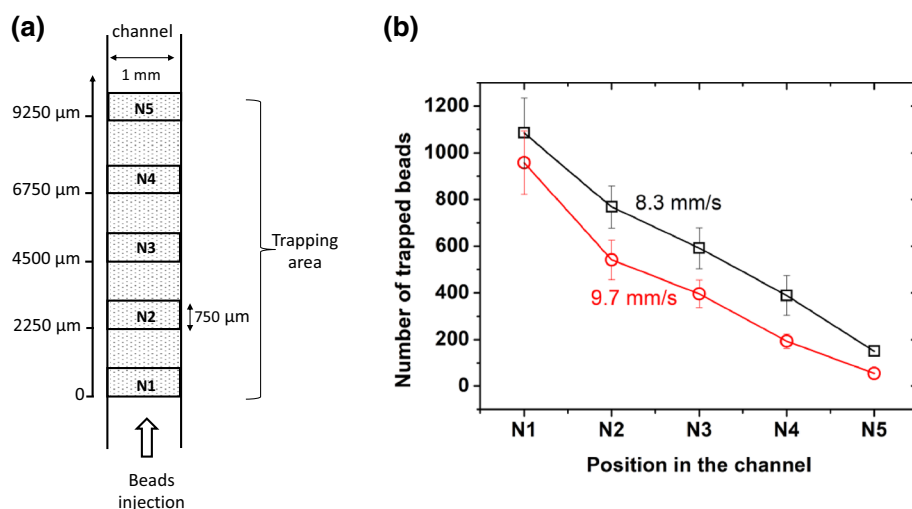
others by bead clusters, as reported in Table 1. The higher fraction of single beads at 9.7 mm/s than at 8.3 mm/s could be attributed to the relatively small cohesion of bead clusters, as expected from dipolar interactions between superparamagnetic beads. Figure 8 reports the ratio of traps occupied by a single bead. This ratio exceeds 50% in the middle of trapping area at 9.7 mm/s, whereas is remains lower than 32% at 8.3 mm/s.

The low cohesion of bead clusters permits to foresee different routes to increase the number of individual trapped beads in the device, notably by modulating the flow rate in time. To illustrate it, we injected beads in the device at lower flow rate, 0.28 μL/s (flow velocity of 2.8 mm/s), in order to fill the entire trapping zone with beads and clusters. Then, to break bead clusters, we created short acceleration through pressure drop by moving capillary. Figure 8b reports a microscopic image of bead trapping in the device. One can observe the absence of large bead clusters and a larger

proportion of single bead trapped. As reported in Fig. 8, the traps occupied by a single bead represent 73–88% of occupied traps. A better control of the short accelerations could permit to precisely monitor the coverage of the microbead array.

4 Conclusion

In this paper, we propose a novel technology to obtain efficient magnetic micro-traps. This novel technology, inspired by composite-polymer approach, is low cost and requires simple fabrication process that breaks with standard microfabrication processes. Developed micro-traps consist of chains of Fe–C microparticles diluted in the PDMS. X-ray tomography experiments gave significantly better insights of microstructure engineering mechanisms for low Fe–C concentration magnetic composites (1 wt% and 5 wt%). The
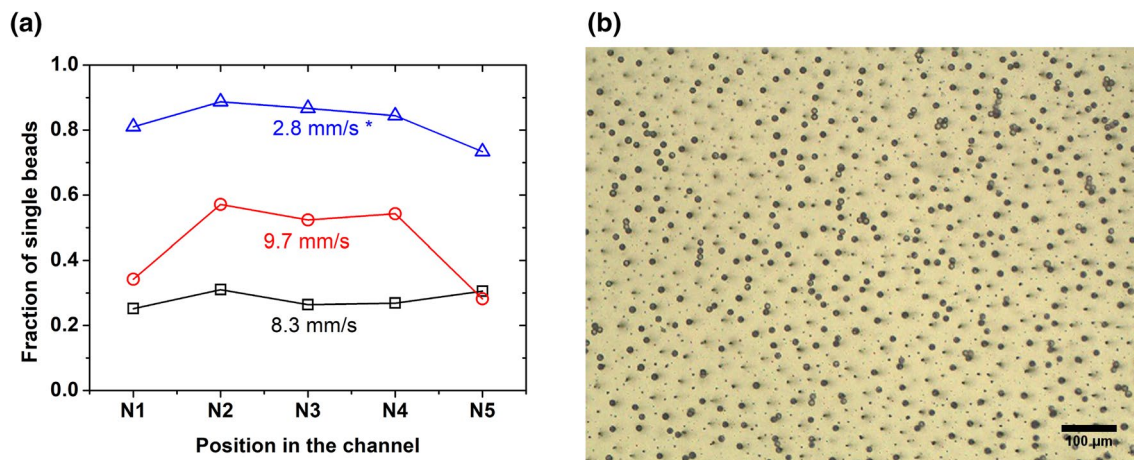

Fig. 8 **a** Fraction of filled traps with a single bead for flow velocities of 8.3 mm/s, 9.7 mm/s and 2.8 mm/s followed by short accelerations. **b** Microscopic images of the trapping area after single bead trapping optimization (and 2.8 mm/s followed by short accelerations)

self-organization of Fe–C particles in a PDMS matrix leads to the creation of highly dense arrays of chain-like agglomerates in large proportion, together with sparse isotropic small agglomerates. Larger traps, originated for 90% of them from CA structure, were identified as the most efficient ones. Their density reached 1300 magnetic micro-traps/mm^2, with diameter from 4 to 11 μm, and an average nearest neighbor distance of 21 μm. They were implemented in a microfluidic channel. Trapping experiments were performed at flow rates ranging from 0.14 to 0.97 μL/s. These first characterized devices demonstrated trapping efficiency superior to 99.7% and permitted to trap up to 750 beads/mm^2. We obtained throughputs as high as 7100 trapped beads/min. This promising technology allows to reach high trapping performances, competitive with hydrodynamic approach, while requiring simple fabrication process and handling.

References

Arnold DP, Wang N (2009) Permanent magnets for MEMS. J Microelectromech Syst 18:1255–1266

Cetin B, Özer MB, Solmaz ME (2014) Microfluidic bio-particle manipulation for biotechnology. Biochem Eng J 92:63–82

Chen P, Huang Y-Y, Hoshino K, Zhang X (2014) Multiscale immunomagnetic enrichment of circulating tumor cells: from tubes to microchips. Lab Chip 14:446–458

Chen H, Sun J, Wolvetang E, Cooper-White J (2015) High-throughput, deterministic single cell trapping and long-term clonal cell culture in microfluidic devices. Lab Chip 15:1072–1083

Coey JMD (2011) Hard magnetic materials: a perspective. IEEE Trans Magn 47:4671–4681

Delapierre F-D, Mottet G, Taniga V et al (2017) High throughput micropatterning of interspersed cell arrays using capillary assembly. Biofabrication 9:015015

Deman A-L, Chateaux J-F, Dhungana D et al (2017) Anisotropic composite polymer for high magnetic forces in microfluidic systems. Microfluid Nanofluidics

Dempsey NM, Walther A, May F et al (2007) High performance hard magnetic NdFeB thick films for integration into micro-electromechanical systems. Appl Phys Lett 90:092509

Dempsey NM, Le Roy D, Marelli-Mathevon H et al (2014) Micromagnetic imprinting of high field gradient magnetic flux sources. Appl Phys Lett 104:262401

Dumas-Bouchiat F, Zanini L-F, Kustov M et al (2010) Thermomagnetically patterned micromagnets. Appl Phys Lett 96:102511

Esmaeilsabzali H, Beischlag TV, Cox ME et al (2016) An integrated microfluidic chip for immunomagnetic detection and isolation of rare prostate cancer cells from blood. Biomed Microdevices 18:22

Faivre M, Gelszinnis R, Degouttes J et al (2014) Magnetophoretic manipulation in microsystem using carbonyl iron-polydimethylsiloxane microstructures. Biomicrofluidics 8:054103

Forbes TP, Forry SP (2012) Microfluidic magnetophoretic separations of immunomagnetically labeled rare mammalian cells. Lab Chip 12:1471–1479

Ghosh S, Puri IK (2013) Soft polymer magnetic nanocomposites: microstructure patterning by magnetophoretic transport and self-assembly. Soft Matter 9:2024–2029

Günther D, Borin DY, Günther S, Odenbach S (2011) X-ray microtomographic characterization of field-structured magnetorheological elastomers. Smart Mater Struct 21:015005

Henighan T, Chen A, Vieira G et al (2010) Manipulation of magnetically labeled and unlabeled cells with mobile magnetic traps. Biophys J 98:412–417

Hosic S, Murthy SK, Koppes AN (2015) Microfluidic sample preparation for single cell analysis. Anal Chem 88:354–380

Jaiswal D, Rad AT, Nieh M-P et al (2017) Micromagnetic cancer cell immobilization and release for real-time single cell analysis. J Magn Magn Mater 427:7–13

Jung Y, Choi Y, Han K-H, Frazier AB (2010) Six-stage cascade paramagnetic mode magnetophoretic separation system for human blood samples. Biomed Microdevices 12:637–645

Khashan SA, Furlani EP (2014) Scalability analysis of magnetic bead separation in a microchannel with an array of soft magnetic elements in a uniform magnetic field. Sep Purif Technol 125:311–318

Kim H, Lee S, Kim J (2012) Hydrodynamic trap-and-release of single particles using dual-function elastomeric valves: design, fabrication, and characterization. Microfluid Nanofluidics 13:835–844

Le Roy D, Shaw G, Haettel R et al (2016a) Fabrication and characterization of polymer membranes with integrated arrays of high performance micro-magnets. Mater Today Commun 6:50–55

Le Roy D, Dhungana D, Ourry L et al (2016b) Anisotropic ferromagnetic polymer: a first step for their implementation in microfluidic systems. AIP Adv 6:056604

Li J, Zhang M, Wang L et al (2011) Design and fabrication of microfluidic mixer from carbonyl iron-PDMS composite membrane. Microfluid Nanofluidics 10:919–925

Marchi S, Casu A, Bertora F et al (2015) Highly magneto-responsive elastomeric films created by a two-step fabrication process. ACS Appl Mater Interfaces 7:19112–19118

McDonald JC, Duffy DC, Anderson JR et al (2000) Fabrication of microfluidic systems in poly (dimethylsiloxane). Electrophor Int J 21:27–40

Mohamadi RM, Besant JD, Mepham A et al (2015) Nanoparticle-mediated binning and profiling of heterogeneous circulating tumor cell subpopulations. Angew Chem 127:141–145

Nam J, Huang H, Lim H et al (2013) Magnetic separation of malaria-infected red blood cells in various developmental stages. Anal Chem 85:7316–7323

Narayanamurthy V, Nagarajan S, Samsuri F, Sridhar T (2017a) Microfluidic hydrodynamic trapping for single cell analysis: mechanisms, methods and applications. Anal Methods 9:3751–3772

Narayanamurthy V, Nagarajan S, Samsuri F, Sridhar T (2017b) Microfluidic hydrodynamic trapping for single cell analysis: mechanisms, methods and applications. Anal Methods

Portemont C (2006) Etude de l'anisotropie d'échange dans des agrégats de cobalt nanométriques, Matiere Condensée [cond-mat]. Université Joseph Fourier-Grenoble I, Français. P. 42

Rampini S, Li P, Lee G (2016) Micromagnet arrays enable precise manipulation of individual biological analyte—superparamagnetic bead complexes for separation and sensing. Lab Chip 16:3645–3663

Rasponi M, Piraino F, Sadr N et al (2011) Reliable magnetic reversible assembly of complex microfluidic devices: fabrication, characterization, and biological validation. Microfluid Nanofluidics 10:1097–1107

Renaud L, Selloum D, Tingry S (2015) Xurography for 2D and multilevel glucose/O$_2$ microfluidic biofuel cell. Microfluid Nanofluidics 18:1407–1416

Royet D, Hériveaux Y, Marchalot J et al (2017) Using injection molding and reversible bonding for easy fabrication of magnetic cell trapping and sorting devices. J Magn Magn Mater 427:306–313

Saliba A-E, Saias L, Psychari E et al (2010) Microfluidic sorting and multimodal typing of cancer cells in self-assembled magnetic arrays. Proc Natl Acad Sci 107:14524–14529

Tekin HC, Gijs MA (2013) Ultrasensitive protein detection: a case for microfluidic magnetic bead-based assays. Lab Chip 13:4711–4739

Xia Y, Whitesides GM (1998) Soft lithography. Angew Chem Int Ed 37:550–575

Xu X, Li Z, Kotagiri N et al (2013) Microfluidic microsphere-trap arrays for simultaneous detection of multiple targets. International Society for Optics and Photonics, p 86151E

Yesilkoy F, Ueno R, Desbiolles B et al (2016) Highly efficient and gentle trapping of single cells in large microfluidic arrays for time-lapse experiments. Biomicrofluidics 10:014120

Yu X, Feng X, Hu J et al (2011) Controlling the magnetic field distribution on the micrometer scale and generation of magnetic bead patterns for microfluidic applications. Langmuir 27:5147–5156

Zanini L-F, Dempsey NM, Givord D et al (2011) Autonomous micromagnet based systems for highly efficient magnetic separation. Appl Phys Lett 99:232504

Zhou R, Wang C (2016) Microfluidic separation of magnetic particles with soft magnetic microstructures. Microfluid Nanofluidics 20:48

Publisher's Note Springer Nature remains neutral with regard to jurisdictional claims in published maps and institutional affiliations.